technische universität dortmund

department of computer science

TECHNICAL REPORTS IN COMPUTER SCIENCE

Technische Universität Dortmund

Signal Analysis and Classification for Plasmon Assisted Microscopy of Nanoobjects

F. Weichert and M. Gaspar and C. Timm and A. Zybin and
E. L. Gurevich and M. Engel and H. Müller and P. Marwedel

Chair VII – Computer Graphics
Chair XII – Embedded Systems
ISAS – Institute for Analytical Sciences

Number: 830
June 2010

Technische Universität Dortmund — Fakultät für Informatik
Otto-Hahn-Str. 14, 44227 Dortmund

F. Weichert and M. Gaspar and C. Timm and A. Zybin and E. L. Gurevich and M. Engel and H. Müller and P. Marwedel: *Signal Analysis and Classification for Plasmon Assisted Microscopy of Nanoobjects,* Technical Report, Department of Computer Science, Technische Universität Dortmund.

ABSTRACT

In this paper we suggest a novel technique for surface plasmon resonance assisted detection of viruses and nanoparticles which can be applied for rapid analysis of large data volumes. The future availability of such an efficient detection method for viruses is evident in terms of globally spreading virus infections. The technique is based on the segmentation of slices, aimed at an automatic identification of nanoparticles, in which detection is based on position-stationary spatiotemporal data using a one dimensional signal-analysis and -classification approach. As data source a CCD camera taking a sequence of snapshots from a surface plasmon assisted microscopy is used. A one dimensional intensity analysis approach is applied for segmentation by classifying time dependent 1D gray level profiles and combining them into spatial 2D segments.

1 INTRODUCTION

The realization of small and portable biosensors becomes increasingly important in the context of medical-biological problems [5]. Particularly in consideration of an increasing demand for epidemic infection control, the availability of an efficient and reliable method for virus detection is evident [15].

One of the most important imaging techniques, which requires rapid data evaluation, is optical microscopy. Optical microscopy is known since the end of the XVI^{th} century and is still one of the main tools in medicine, physics and biology. Since then many modifications and improvements of optical microscopy have been suggested, e.g. dark field microscopy, phase contrast microscopy, confocal microscopy and surface plasmon microscopy (SPR-microscopy). SPR-microscopy, first suggested in [19], has found plenty of applications, see e.g. [13, 24, 18, 7, 11, 21]. The method is based on detection of light reflected from a thin metal film (the *sensor*), in which a surface plasmon wave is excited. It is well known that the lateral resolution of this method is about 20 μm, which is determined by the plasmon propagation length. Therefore the method is usually applied to examining the lateral structures of 100 μm and more [20, 2].
A significant improvement is given by the novel PAMONO technique (Plasmon assisted Microscopy of Nano-Size Objects). The PAMONO technique allows the detection of nanosized objects such as dielectric particles down to several tens of nanometers or viruses as it was recently demonstrated by the authors [27]. It furthermore provides the opportunity to detect selectively particles of interest and by this it offers a significant extension of application areas of SPR microscopy. A more detailed description of these facts is given in section 2. However, the new technique requires corresponding new efficient identification algorithms and system for processing the data.

This requires in addition a specialized microsystem capable of managing the large amount of data and an image acquisition which is capable of detecting nanoparticles characterized by low signal amplitudes on a noisy background, i.e. by low signal to noise ratio (SNR). The volume of the data depends on the bit rate of the CCD chips' ADC [16], the number of processed pixel and the frame rate. These parameters are crucial for the detection power of the sensor: Higher bit rates result in better sensitivity of the detection; a large number of processed pixel allows increasing the studied area and the SNR; high frame rates allow observation of rapid processes and increasing the SNR by means of averaging [4].

The structure of the signal processing pipeline, which is described in the following sections, enables the processing system to work on the data massively in parallel and thus a system of several independently working processing pipeline steps was designed. A portable system has strong constraints for designing the system, e.g. weight and energy efficiency. "Field programmable gate arrays"(FPGA) are reconfigurable hardware devices increasingly used in embedded systems to create energy and performance optimized designs without the high cost implied by custom hardware designs (e.g. [14]). Recent

FPGAs include special functional blocks for improved digital signal processing (DSP) capabilities which are useful to create hardware-accelerated functional blocks, e.g. for efficiently implementing signal processing transformations like S-Transforms or DCTs [17].

The paper is organized as follows: Section 2 introduces the experimental setup, section 3 presents the concept of an automatic identification of nanoparticles and section 4 shows the architecture of an embedded signal processing system. Following, section 5 shows exemplary results that are obtainable using the presented analysis and section 6 concludes with some remarks on the current state and the further development.

2

PAMONO TECHNIQUE

The PAMONO technique setup which is based on the SPR microscopy (Kretschmann configuration [12]) in imaging mode [19] is used for the experiments (see Figure 2.1). A superluminescsent diode QSDM-680-9 (QPhotonics) with the wavelength λ=670 nm power 10 mW, linewidth 10 nm is applied to excite surface plasmon resonance (SPR) in a 50 nm thick gold layer (the *sensor*) deposited on a glass prism. The gold detecting layer is illuminated through the prism at a fixed incidence angle of approximately 60^0 chosen to maximize the sensitivity of the method [26]. The reflected light is projected onto the 12-Bit *Kappa DX 40 - 1020 FW* CCD camera by means of Minolta photo objective f=50 mm with 1000×1000 pixel of $7.4\times7.4\,\mu$m and full-well pixel capacity of 42000 electrons was used. An area of 0.2 square millimeters can be recorded with the frame rate of approximately 50 fps (frames per second). The nanoparticles or viruses are injected in the flow of distilled water or in PBS buffer (Phosphate Buffered Saline), which is pumped through the microfluidic flow cell contacting the detector by means of a peristaltic pump with the flow rate of 300 μL/min. The volume of the microfluidic cell used in our experiments is approximately 300 μL. A particle being in the vicinity of the surface is bound to the gold layer coated by corresponding selective receptors.
Biotinilated monoclonal antibodies *2G12* were immobilized on the gold surface which was already covered with a streptavidin monolayer. The reflection from the gold surface increases locally, resulting in a bright spot appearing on the monitor, see Figure 2.2. Though the technique is based on the conventional SPR microscopy it enhance the technique by a few significant facts.

The conventional SPR microscopy is able to detect variations of effective layer thickness in picometer range which provides very high analytical sensitivity. However this method suits well for measurements, in which the analyst creates a layer of definite thickness on the sensor surface. Detection and counting of individual analytical agents is supposed to be impossible. Recently it was demonstrated that slightly modified SPR microscopy provides a possibility to

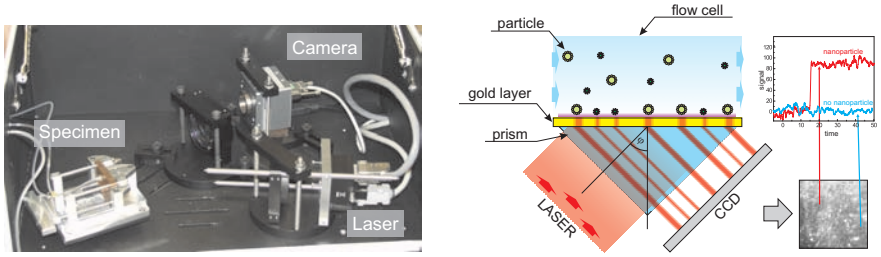

(a) PAMONO-Sensor (b) schematic setup

Abbildung 2.1: Experimental setup of the PAMONO-Sensor: (**a**) photo of the setup and (**b**) schematic illustration.

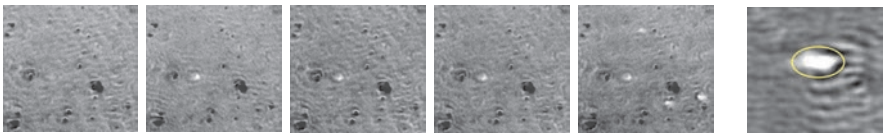

(a) (b) (c) (d) (e) (f)

Abbildung 2.2: Five consecutive snapshots (**a**)-(**e**) of 80 nm polystyrene nanoparticles emerging on the detector surface and (**f**) a magnified nanoobject. The background is removed and the snapshots are averaged over 50 frames in order to make the particles visible.

detect immediately binding of individual nano-size particles on the sensor surface. The novel PAMONO technique exploits a phenomenon of local reflectivity increasing caused by a particle attached to the gold layer. Polystyrene spheres of 40 nm in diameter were detected with the signal/noise ratio of $\sim$5. Since the size-signal dependence is approximately linear, particles down to 10 nm can be detected provided that the dependence remains unchanged for particles below 40 nm. This offers a significant extension of application areas of SPR microscopy.

The detection of nano-size particles is possible due to excitation of concentric plasmon waves by interaction of a particle with the evanescent field near to the gold layer. As a result a local increase in the reflection is caused by a particle bound to the detector surface These concentric waves were observed and investigated by means of near field microscopy in [25, 9]. The far field radiation caused by such plasmons is obviously responsible for the bright spot on the image. Any bound particle manifests itself as a bright spot on the surface image so that the number of bound particles can be counted (see Figure 2.2). This number can be taken for characterization of the particle concentration in a liquid sample instead of the averaged layer thickness taken by conventional SPR microscopy. However a quantitative theory of the far field radiation is still not available.

The PAMONO technique provides the opportunity to detect selectively particles of interest. For example coating the sensor surface with antibodies to a definite virus provides selective detection of only this type of viruses. Unlike the electron microscopy the method does not require vacuum: The studied object may be surrounded by gas, liquid or vacuum. Therefore the object of interest can be studied at the natural environment and the binding process can be monitored live. Unlike any other method, the nanoparticles can be simply counted similar as microobjects are counted by conventional microscopy.

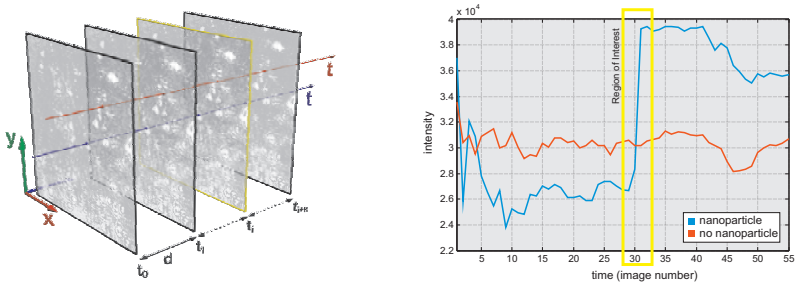

(a) Image sequence

(b) Intensity series

Abbildung 2.3: Schematic representation of the experimental setup for nanoparticle detection: (**a**) Image sequence and (**b**) Comparison of the temporal intensity variation at two exemplary image positions: a virus adhering to the detector surface results in an erratic increase.

3

IMAGE PROCESSING

Figure 2.3 shows the concept of automatic nanoparticle detection, which is based on the analysis of the image sequence (figure 2.3(a)) regarding characteristic temporal and spatial intensity variations.
In effect, the main criteria for the identification of a nanoparticle or virus are:

- A particle bound to the sensor results in a bright spot (compared to its local neighborhood).
- The spot appears after the particles are injected into the cell and bound on the gold layer. There are diverse spots present from the beginning, which are referred to the background.
- The spot does not move after the binding. The intensity of the spot measured as a function of time looks like a step of a certain height, see Figure 2.3(b).
- The height of the step (see Figure 2.3(b)) or the intensity of the spot should correspond to the average intensity, which is determined in preliminary experiments with calibrated particles of interest.

Regarding these characteristics, the proposed automatic particle identification considers the evolution of pixel intensities in time by means of a signal analysis pipeline. Beforehand, some image preparation needs to be done to render the immanent particles distinguishable from the background at all, as described in section 3.1. The subsequent particle identification is divided into two steps, namely the identification of all pixel that contribute to particles (section 3.2) and the aggregation of these pixel into segments that represent distinct particles (section 3.3).

3.1 BACKGROUND CORRECTION AND FILTERING

At first the background is removed in order to separate relevant intensity patterns from irrelevant variations caused by experimental setting properties. Simplistically assuming a stationary background allows a constant reference image to be used for background removal, which is constructed by averaging the first B images (e.g. B=20). In order to eliminate broad intensity fluctuations stemming from a background which actually is nonstationary, the intensity average and variance of each image is standardized to decrease misclassifications caused by systematical intensity peaks. An appropriate average and variance value is determined by pretesting a small sample of images. Based on these preliminary inquiries average and variance are set to 30000 and 3000, respectively, to approximately cover the full range of 16bit images[1].
An alternative approach models the background nonstationary by updating suitable intensity statistics of each background pixel at each new frame of the

1 although the camera's bit rate is 12, processing is performed using 16bit images

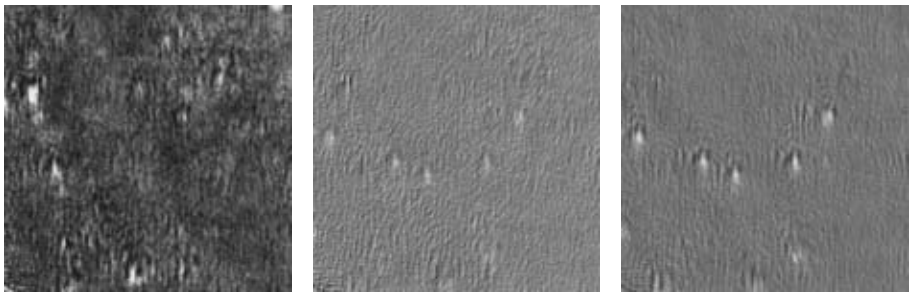

(a) Raw image (b) Constant background removed (c) Sliding background removed

Abbildung 3.1: Comparison of different approaches for background removal

dataset. This in turn allows for a compensation of systematical temporal intensity variations and slowly emerging obstacles. The term *obstacles* shall denote all sources of temporal intensity variations that are not caused by the binding of a relevant particle to the detector surface. By limiting the updated background intensity statistics to an intensity average, a sliding background image is applied, which is computed by averaging B images foregoing the currently analyzed image with a predefined temporal offset. Via caching the B foregoing images in main memory, the run-time is insignificantly slower than the constant background case.
Figure 3.1 shows a cutout of the raw image along with its background corrected versions using a constant and a sliding background. Note the invisibility of resulting spots in the raw image. Figure 3.2 shows intensity curves at exemplary particle positions with a constant and sliding background removal in comparison. As can be seen, sharper peaks are obtainable via a nonstationary background correction, but the characteristic intensity step drops off after the emergence of a particle, due to its incorporation into the sliding background. This fact complicates the distinction between flashing obstacles and relevant particles.

An important observation is that particles exhibit not only a temporal but also a spatial extent, resulting in a number of neighboring pixel showing similar intensity curves. This characteristic collective intensity variation is crucial in the separation of relevant variations from image noise and is exploited by means of a median filter applied to each background corrected image, which eliminates temporal variations with too little spatial extent. A more advanced exploitation of the collective intensity variation is part of current work and discussed in section 6.

3.2 IDENTIFICATION OF PARTICLE PIXEL

After background correction, normalization and filtering, the dataset is segmented in a region growing manner by classifying each pixel independently using its time dependent intensity variation. In order to avoid an exhaustive signal analysis at every single pixel, particle candidate pixel (pcp) are identified

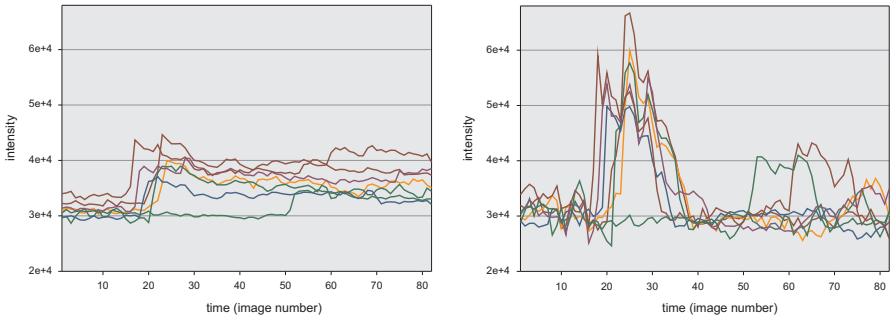

(a) Constant background (b) Sliding background

Abbildung 3.2: Temporal intensity curves at 7 particle positions using constant and sliding background

beforehand, which are characterized by an intensity that exceeds some predefined threshold at any point in time. Only these pcp's are regarded as potential particle positions by further analysis and classification, since the maximum intensity of non-pcp's is too low at all to represent the binding of a particle to the detector surface at any point in time.
The resulting pcp's can now be divided into relevant particle positions and irrelevant obstacles by means of a signal analysis approach.

In order to enable classification, discriminative features need to be constructed that are able to distinguish the underlying image content. As described above, simple intensity properties can be used to reduce the search space via generation of particle candidate pixel that need further analysis and direct rejection of non-candidate pixel. The usage of a weak yet fast extracted feature to identify candidates is crucial to allow application of stronger yet computationally expensive features for final classification due to the small fraction of particle pixel.

Particle candidates may be classified using features generated from a broad range of analytical, spectral or statistical signal analysis approaches. The presented approach exemplarily uses a weighted combination of running differences with temporal averaging window, as well as coefficients of a time-frequency representation named S-Transform. The latter is computed by [23, 22]:

$$S_f(t_0,k) = \begin{cases} \frac{1}{N}\sum_{t=0}^{N-1} f(t) & \text{for} \quad k=0 \\ \sum_{m=0}^{N-1} F(m+k)\cdot e^{-\frac{2\pi^2 m^2}{k^2}} \cdot e^{i2\pi\frac{m}{N}t_0} & \text{for} \quad k=1,\ldots,N-1 \end{cases} \tag{1}$$

with $f(t)$ a discrete signal of length N and $F(k)$ its Fourier transform, $t_0 \in \{0,\ldots,N-1\}$ and $k \in \{0,\ldots,\lceil N/2 \rceil\}$. Comparable to a windowed Fourier transform, the S-Transform computes correlations of the discrete function $f(t)$ and translated and frequency-modulated Gaussian windows, with translation and modulation being indexed by parameters t_0 and k. Figure 3.3 shows the magnitudes of the S-Transform representations of the two intensity curves of

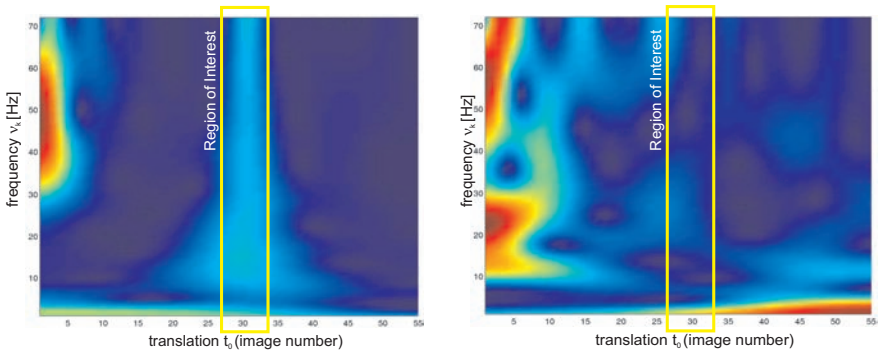

(a) Nanoparticle (b) No nanoparticle

Abbildung 3.3: Magnitudes of Time-frequency representations of the to intensity curves of Figure 2.3(a) in comparison.

figure 2.3(a) computed by equation 1. The abscissa shows the temporal translation t_0 of the analysis window and the ordinate its corresponding frequency ν_k in units of Hz, which is given by $\nu_k = k/\left(N\Delta T\right)$, with $\Delta T = 1/40s$. As can be seen, the presence of intensity variations of particular duration results in peaks or ridges at corresponding locations in the time-frequency domain. The region of high magnitudes on the left of both images results from an inhomogeneous oscillatory illumination at the beginning of the record, which the normalization was not able to compensate. In fact, the maximum magnitude of the particle case is significantly higher than that of the non-particle case.

The extracted particle candidates are accepted as particles or rejected as particle-free position based on their similarity to the corresponding class prototype using the spectral and analytical features as described above.

3.3 PARTICLE AGGREGATION

As stated above, particles exhibit a characteristic temporal as well as spatial extent. This fact was exploited during image filtering to eliminate particle-like intensity variations with a spatial extent being too small to be considered particles. The second utilization of the spatial extent consists of an aggregation of neighboring particle pixel into a single particle segment, and a subsequent filtering of resulting segments using features of shape. Therefore, neighboring particle pixel are aggregated by means of a single closed polygon. As mentioned above, due to the characteristic spatial extent of relevant particles, a concluding selection rejects irrelevant obstacles with particle-like temporal intensity variations based on the following two features of shape [10]:

$$\text{polygon area:} \quad A = \frac{1}{2}\sum_{i=0}^{n-1}\left(x_i y_{i+1} - x_{i+1} y_i\right) \tag{2}$$

$$\text{circularity:} \quad C = \frac{4\pi A}{P^2}, \tag{3}$$

in which n is the number of polygon nodes, (x_i, y_i) the coordinates of the i-th node and P the polygon perimeter. The choice of the features of shape is

motivated by the fact that irrelevant obstacles which persist the particle pixel identification, result in segments that are either too big or unshaped to represent a bound particle. The shape-based filtering of segments then allows the rejection of these segments despite their particle-like temporal intensity curves.

Since real applications of the presented approach have demands of time-critical and energy-efficient execution, the next section treats its implementation in specialized hardware.

Section 5 will show the applicability of the introduced particle identification pipeline in terms of accurate particle detection. But for mass screening it is important to realize small and portable biosensors. This coincides with microsystems which combines Smart Cameras with FPGAs as an integrated signal processing system. The overall design of such a microsystem is depicted in Figure 4.1. The images provided by the CCD camera are transferred via a high speed bus to the microsystem [16], where they are stored in the main memory for further processing. The results of the signal processing pipeline can be transferred from main memory to a hard disk or/and to a display. The signal is processed in several independently and concurrently working pipelines which utilize the main memory for data communication between the pipeline steps.

The different signal processing pipeline elements are mapped to the pipeline as depicted in Figure 4.1. The first element of the pipeline implements the background correction, the second one the denoising and the last element of the pipeline handles the signal analysis. As can be seen several concurrently working cores of one pipeline step can process the image data highly in parallel by using different parts of the images.

The microsystem main processing unit is an FPGA which is flexible and suited for sequenced signal processing tasks. Since FPGAs allow for imple-

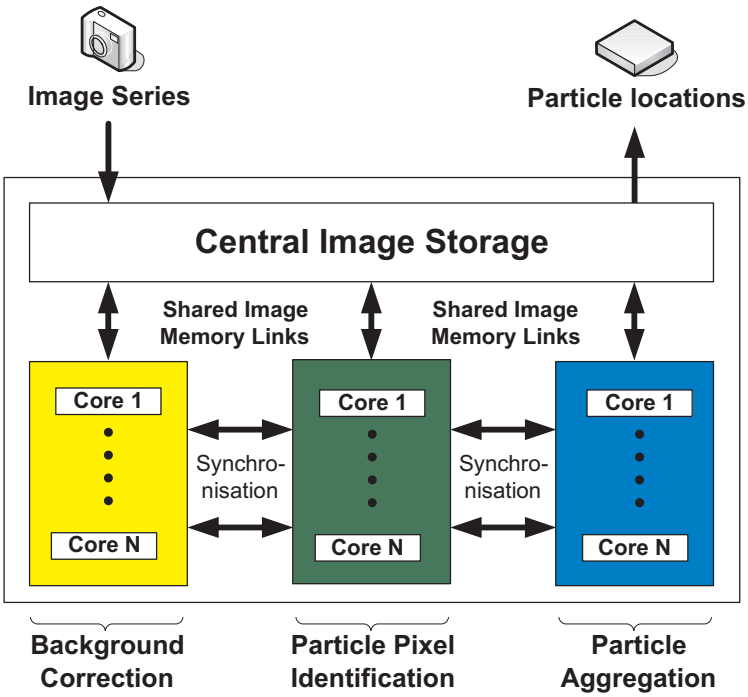

Abbildung 4.1: Pipeline on reconfigurable hardware (FPGA)

mentation of arbitrary logic functions, signal processing tasks can be divided into performance-critical tasks implemented in dedicated hardware units and administrative tasks implemented in software on a CPU created on the FPGA. The microsystem approach uses LavA [1], a system to simultaneously configure a multi-core/many-core processing system and the required system software components to support the image processing application. In order to relieve the application developer from the burden of hardware design, a high-level feature model describing the required functionality (e.g., CPUs, signal processing hardware units, memory, synchronization elements) is used as an input to the configuration process. The result of this configuration process is a VHDL hardware description directly usable to configure an FPGA and a set of software libraries to support the application, e.g., by implementing synchronization and communication primitives. If sufficient space is available on the FPGA, this approach also permits the implementation of multiple pipelines operating on different parts of one image or different images in parallel in order to speed up processing.

Using the LavA configuration approach, the system designer is enabled to shift functionality from hardware to software and vice versa. This makes it easy to optimize the performance of the system for a given application considering FPGA space and cost constraints typical in embedded systems. In addition, relying on a high-level specification allows for rapid adaptation of the system to FPGA technologies from different vendors.

5 RESULTS

The particle identification was evaluated on four types of datasets using specimen of predefined composition, whereof two sets used virus-like-particles (VLP) of different origin and the other two used synthetic particles of a predefined size of 80nm and 200nm. Particularly the VLP's are equal to real viruses in their external structure and size, but they do not contain any genetic material and, therefore, can be safely used in experiments [8]. The raw data consists of a total amount of 4704 images, divided into the four types of datasets containing 1081, 868, 2367 and 388 images, as referred to below.

Figure 5.1 shows intermediate results of the three described steps of particle identification applied to a background corrected cutout and figure 5.2 shows exemplary final results of the particle identification.
A quantitative evaluation of segmentation results is complicated, in that a pixel- or area-based error measure is useless due to diffuse borders between particles and the background - only the similarity to an arbitrary out of a huge set of possible reference segmentations would be measured (cf. Figure 5.2(a)). Therefore, only intersections of extracted and manually defined reference polygons are used for quantitative evaluation of identification results: intersections of extracted and reference polygons are counted as true-positives (tp), non-intersected extracted polygons as false-positives (fp) and non-intersected reference polygons as false-negatives (fn) [6]. True-negatives can not be unambiguously defined this way, because they would be based on polygons that are not extracted and not intersected. Therefore the measures precision and recall are used to evaluate results.
The manually defined reference polygons are constructed beforehand by a human expert observer, who outlines all relevant particles in a dataset to the best of his knowledge.

An exemplary segmentation result for a VLP-dataset is shown in Figure 5.2(b). A quantitative evaluation yields a recall (tp-rate) of 0.85 with 17 tp's and 3 fn's and a precision of 0.61 with 11 fp's. The second VLP-dataset yields a recall of

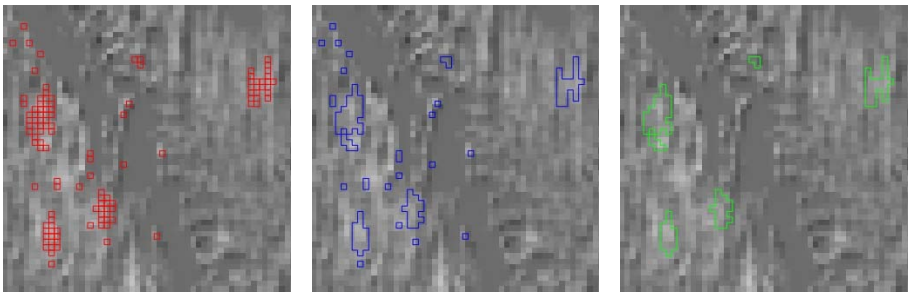

(a) Per pixel identification (b) Polygons constructed (c) Final segmentation

Abbildung 5.1: Results of intermediate particle identification steps

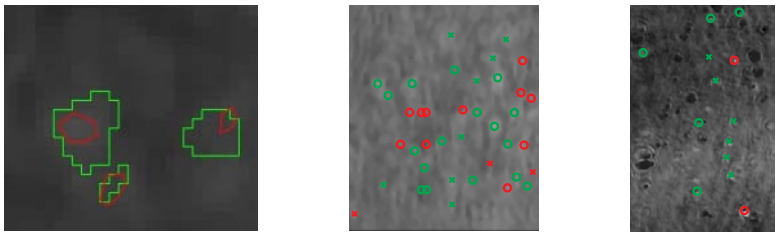

(a) Cutout of segmentation (b) Virus-Like-Particles (c) synthetic particles (80nm)

Abbildung 5.2: Particle identification result: (**a**) reference polygons are red and extracted polygons green; (**b**) and (**c**) circles mark identified particles and crosses regions with no recognized particle. Green marks are correct and red incorrect identifications of the pixel class. Red circles are false alarms, red crosses unrecognized particles and green crosses correctly rejected candidates.

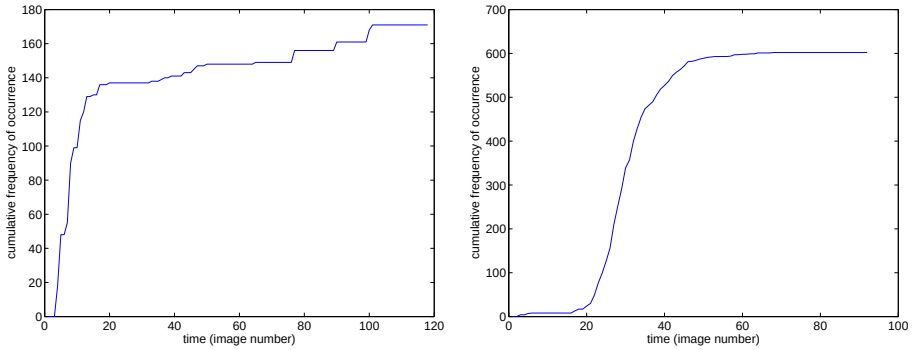

(a) synthetic 80nm (b) synthetic 200nm

Abbildung 5.3: Cumulative frequency of particle pixel as a function of image number

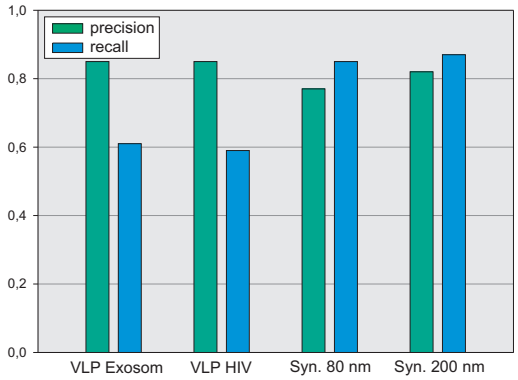

Abbildung 5.4: Evaluation results (precision/recall) of four types of datasets using specimen of predefined composition, whereof two sets used virus-like-particles (VLP) of different origin and the other two used synthetic particles of a predefined size of 80nm and 200nm

0.85 with 29 tp's and 5 fn's and a precision of 0.59 with 20 fp's. Both precisions point to a yet too high rate of false alarms. An exemplary segmentation cutout of the alternative evaluation based on synthetic particles of predefined size is shown in Figure 5.2(c). The 80nm-case yields a recall of 0.77 with 17 tp's and 5 fn's and a precision of 0.85 with 3 fp's, which points to a low rate of false alarms. The 200nm-case yields a recall of 0.82 with 27 tp's and 6 fn's and a precision of 0.87 with 4 fp's. In summary, cf. Figure 5.4, the identification of synthetic particles produced a significantly lower rate of false alarms than the identification of VLP's, which is primarily caused by a yet significantly varying image quality. The recall is comparable in both settings with an insignificant benefit in the VLP-case.

Examining the source of misses and false alarms, a great potential lies in an improved background correction, since distracting artifacts are introduced into the identification process by treating an actually nonstationary background as stationary. Furthermore, the exploitation of the spatiotemporal extent of relevant particles can be improved by using multivariate signal analysis, since the univariate temporal intensity variation at a single position is often ambiguous. Lastly, figure 5.3 shows the cumulative frequency of particle pixel occurrence as a function of image number for the two synthetic particle datasets. Since the beginning of record and particle injection have not yet been synchronized, a temporal lag between the curves is not yet evaluable, but the different slope of increase of bound particles is easily visible.

The evaluation of the signal processing algorithms is only one part of the microsystem design. A second part comprises the analysis of important performance indicators of the hardware signal processing pipeline. Therefore figures 5.5(a) and 5.5(b) show the impact of different algorithm parameters on the runtime of the pipeline respectively the stability of the throughput provided by the microsystem. Figure 5.5(a) details the impact on the runtime by varying the number of images utilized by pipeline steps "background correctionänd "parti-

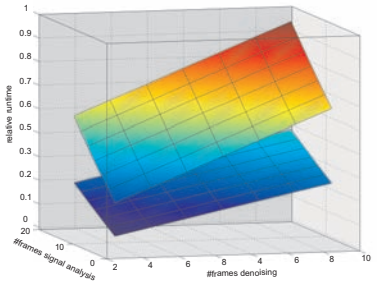

(a) Pipeline Runtime for different Parameters

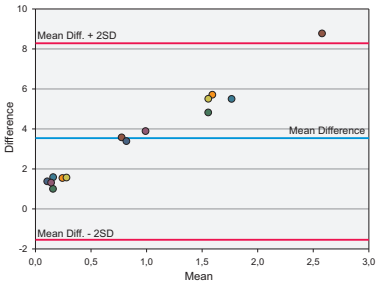

(b) Stability of Pipeline Throughput

Abbildung 5.5: Microsystem Design Results

cle pixel identification". Furthermore different numbers of cores are chosen for realizing the pipeline which results in the two planes in the plot. The upper plane illustrates the case if each pipeline step utilizes one core and the lower plane illustrates if a pipeline step utilizes two cores. In summary one can say that the pipelines runtime scales with the number of cores which means to get a higher throughput one have to increase the number of cores. Figure 5.5(b) depicts a Bland-Altman plot [3] with the deviation of the measured best case runtimes and worst case runtimes from the average runtimes. As one can see the average difference of the best case and worst case runtimes is below 4, which means in our case that best and worst case runtimes differ on average by two percent.

6 DISCUSSION

The paper demonstrates an automated and effective approach to nanoparticle and virus identification. In view of an increasing demand for epidemic infection control, the availability of an efficient detection method for viruses is evident. The detection method is based on raw data acquired from the novel PAMONO technique. Dependent on the experimental setting, a background is removed by means of either a constant or a sliding background image, which are initialized using the leading part of the raw data. This step is essential and benefits from further development, since relevant particles are invisibly and inseparably hidden in a complex but irrelevant nonstationary scene resulting from the experimental setting. The subsequent identification of particle pixel candidates significantly reduces the number of positions to analyze and classify, since most positions are dominated by temporal intensity variations below a critical threshold that indicates a possible particle binding. Resulting particle regions are filtered via features of shape to incorporate prior knowledge about the spatial extent of particles, like a minimum size of e.g. four pixel. An objective quantitative evaluation is still complicated due to a difficult and ambiguous definition of reference segmentations to compare against.
The parallel nature of the image processing and particle identification process allows implementation on specialized hardware. The approach was validated on four different types of datasets up to now, and several comments on ongoing development were given to enhance identification accuracy. The hardware design enables processing the image series in parallel and is implemented on an energy efficient and small size FPGA. Furthermore the design is configurable in a way that future improvements and enhancements of the signal processing and particle extraction algorithms can easily be implemented on the chip and tested on real hardware without a great effort. The hardware architecture is also supposed to work with other optical sensor systems in the future.
Besides algorithmic and architectural improvements, the bounding and imaging processes itself need further investigations: one can see from the images that a bound nanoparticle appears as a bright spot surrounded by circles of lower intensities than the background. Such a dark ring resembles a diffraction pattern of a point-like source but is asymmetric and essentially larger than expected. The nature of this pattern is a subject of further study, as well as its utilization in order to increase detection precision.
In summary, the paper shows that the design of a portable biosensor is feasible. The emergence of FPGAs in Smart Cameras sets the trend for small optical biosensors utilizable for mass screening at airports to curtail the global spreading in terms of virus infections.

ACKNOWLEDGMENT

The authors would like to thank V. Temchura (Department of Molecular and Medical Virology, Ruhr-Universität Bochum, Germany) for delivering of the virus-like-particles (VLP's)

[1] Lava: A runtime platform for application-specific distributed architectures.

[2] C.E.H. Berger, R.P.H. Kooyman, and J. Greve. Surface plasmon propagation near an index step. *Opt. Commun.*, 167:183–189, 1999.

[3] J.M. Bland and D. G. Altman. Statistical methods for assessing agreement between two methods of clinical measurement. *Lancet I*, pages 307–310, 1986.

[4] A. Buades, B. Coll, and J.M. Morel. A review of image denoising algorithms with a new one. *Multiscale Model. Simul.*, 4(2):490–530, 2005.

[5] D. Erickson, S. Mandal, A. Yang, and B. Cordovez. Nanobiosensors: optofluidic, electrical and mechanical approaches to biomolecular detection at the nanoscale. *Microfluid. Nanofluid.*, 4(1):33–52, 2008.

[6] T. Fawcett. ROC Graphs: Notes and Practical Considerations for Data Mining Researchers, 2003.

[7] E. Fu, J. Foley, and P. Yager. Wavelength-tunable surface plasmon resonance microscope. *Rev. Sci. Instr.*, 74:3182–3184, 2003.

[8] E.V. Grgacic and D. A. Anderson. Virus-like particles: passport to immune recognition. *Methods*, 40:60, 2006.

[9] B. Hecht, H. Bielefeldt, L. Novotny, Y. Inouye, and D. W. Pohl. Local excitation, scattering, and interference of surface plasmons. *Phys. Rev. Lett.*, 77(9):1889–1892, 1996.

[10] J. Iivarinen, M. Peura, J. Särelä, and A. Visa. Comparison of Combined Shape Descriptors for Irregular Objects. *8th British Machine Vision Conference, BMVC'97*, pages 430–439, 1997.

[11] A. V. Kabashin, V. E. Kochergin, and P. I. Nikitin. Surface plasmon resonance bio- and chemical sensors with phase-polarisation contrast. *Sens. Actuat. B*, 54:51–56, 1999.

[12] E. Kretschmann. Determination of optical constants of metal by excitation of surface plasmons. *Z. Phys.*, 241:313–324, 1971.

[13] H. J. Lee, D. Nedelkov, and R. M. Corn. Surface plasmon resonance imaging measurements of antibody arrays for the multiplexed detection of low molecular weight protein biomarkers. *Anal. Chem.*, 78:6504–6510, 2006.

[14] W.J. MacLean. An evaluation of the suitability of fpgas for embedded vision systems. *Proceedings of the 2005 IEEE Computer Society Conference on Computer Vision and Recognition (CVPR'05)*, 2005.

[15] J. Mairhofer, K. Roppert, and P. Ertl. Microfluidic systems for pathogen sensing: A review. *Sensors*, 9:4804–4823, 2009.

[16] P. Marwedel. *Embedded System Design*. Springer, 2007.

[17] A.M. Patino, M.M. Peiro, F. Ballester, and G. Paya. 2d-dct on fpga by polynomial transformation in two-dimensions. In *Circuits and Systems, 2004. ISCAS '04. Proceedings of the 2004 International Symposium on*, volume 3, pages III–365–8 Vol.3, May 2004.

[18] M. Piliarik and J. Homola. Self-referencing spr imaging for most demanding high-throughput screening applications. *Sens. Actuat. B*, 134:353–355, 2008.

[19] B. Röthenhäuser and W. Knoll. Surface plasmon microscopy. *Nature*, 332:615, 1988.

[20] B. Röthenhäuser and W. Knoll. Surface plasmon interferometry in the visible. *Appl. Phys. Lett.*, 52:1554–1556, 1998.

[21] J. S. Shumaker-Parry, M. H. Zareie, R. Aebersold, and C. T. Campbell. Microspotting streptavidin and double-stranded dna arrays on gold for high-throughput studies of protein-dna interactions by surface plasmon resonance microscopy. *Anal. Chem.*, 76:918–929, 2004.

[22] R.G. Stockwell. *S-Transform Analysis of Gravity Wave Activity from a Small Scale Network of Airglow Imagers*. PhD thesis, University of Western Ontario, 1999.

[23] R.G. Stockwell, L. Mansinha, and R.P. Lowe. Localization of the complex spectrum: The s transform. *IEEE Transactions on Signal Processing*, 44(4):998–1001, 1996.

[24] R. Thariani and P. Yager. Novel, high-quality surface plasmon resonance microscopy. *Sens. Act. B*, 130:765–770, 2008.

[25] P. J. Valle, E. M. Ortiz, and J. M. Saiz. Near field by subwavelength particles on metallic substrates with cylindrical surface plasmon excitation. *Opt. Comm.*, 137:334–342, 1997.

[26] A. Zybin, D. Boecker, V. M. Mirsky, and K. Niemax. Enhancement of the detection power of surface plasmon resonance measurements by optimization of the reflection angle. *Anal. Chem.*, 79:4233–4236, 2007.

[27] A. Zybin, Y. A. Kuritsyn, E. L. Gurevich, V. V. Temchura, K. Überla, and K. Niemax. Surface plasmon resonance for detection of dielectric nanoparticles and viruses. *Plasmonics*, 5:31–35, 2010.